ADVANCED FUNCTIONAL MATERIALS
www.afm-journal.de

Nondestructively Visualizing and Understanding the Mechano-Electro-chemical Origins of "Soft Short" and "Creeping" in All-Solid-State Batteries

*Daxian Cao, Kena Zhang, Wei Li, Yuxuan Zhang, Tongtai Ji, Xianhui Zhao, Ercan Cakmak, Juner Zhu, Ye Cao, and Hongli Zhu**

All-solid-state Li-metal batteries (ASLMBs) represent a significant breakthrough in the quest to overcome limitations associated with traditional Li-ion batteries, particularly in energy density and safety aspects. However, widespread implementation is stymied due to a lack of profound understanding of the complex mechano-electro-chemical behavior of Li metal in the ASLMBs. Herein, operando neutron imaging and X-ray computed tomography (XCT) are leveraged to nondestructively visualize Li behaviors within ASLMBs. This approach offers real-time observations of Li evolutions, both pre- and post- occurrence of a "soft short". The coordination of 2D neutron radiography and 3D neutron tomography enables charting of the terrain of Li metal deformation operando. Concurrently, XCT offers a 3D insight into the internal structure of the battery following a "soft short". Despite the manifestation of a "soft short", the persistence of Faradaic processes is observed. To study the elusive "soft short" , phase field modeling is coupled with electrochemistry and solid mechanics theory. The research unravels how external pressure curbs dendrite growth, potentially leading to dendrite fractures and thus uncovering the origins of both "soft" and "hard" shorts in ASLMBs. Furthermore, by harnessing finite element modeling, it dive deeper into the mechanical deformation and the fluidity of Li metal.

1. Introduction

Reviving the Lithium (Li) metal anode for rechargeable batteries is the optimal solution to address the requirements for high energy density, however, Li metal possesses poor cycling stability and poses significant safety risks due to the dendrite formation during continuous plating and stripping.[1] Using rigid solid-state electrolytes (SEs) was once thought to suppress dendrite growth. Yet, all-solid-state Li-metal batteries (ASLMBs) failed even faster than Li-metal batteries using conventional liquid electrolytes.[2] Many studies have reported that Li metal can propagate through SEs along grain boundaries,[3] cracks,[4] and voids.[5] The relatively high electrical conductivity of SE can also trigger Li deposition inside the SE.[6] Therefore, for better battery designs, it is critical to have a thorough understanding of the Li behavior and the short circuit phenomenon in the ASLMBs.

As the most common ASLMB failure, the short circuit can be classified as either a "hard short" or "soft short" (also known as a soft breakdown). In the case of a "hard short", the voltage decreases dramatically during the charging process. This is the most common short circuit, and the battery cannot be recovered. In contrast, a "soft short" phenomenon has been frequently observed in ASLMBs, yet it has not been well understood. In "soft short", the battery voltage dynamically maintains stability but cannot increase during the charging process. Under certain circumstances, the

D. Cao, W. Li, T. Ji, J. Zhu, H. Zhu
Department of Mechanical and Industrial Engineering
Northeastern University
Boston, MA 02115, USA
E-mail: h.zhu@neu.edu

The ORCID identification number(s) for the author(s) of this article can be found under https://doi.org/10.1002/adfm.202307998

DOI: 10.1002/adfm.202307998

K. Zhang, Y. Cao
Department of Materials Science and Engineering
The University of Texas at Arlington
Arlington, TX 76019, USA

Y. Zhang
Neutron Scattering Division
Oak Ridge National Laboratory
Oak Ridge, TN 37831, USA

X. Zhao
Environmental Science Division
Oak Ridge National Laboratory
Oak Ridge, TN 37831, USA

E. Cakmak
Materials Science and Technology Division
Oak Ridge National Laboratory
Oak Ridge, TN 37831, USA

battery is capable of recovering from this short circuit.[7] In some Li|SE|Li symmetric cells, the "soft short" can enable deceptive cycling stability, which is difficult to find out and may deliver improper conclusions. Wang et al. recently highlighted the deceptive cycling stability caused by the "soft short" in ASLMBs and suggested using electrochemical techniques, such as cyclic voltammetry and electrochemical impedance spectroscopy, to diagnose the "soft short".[8] However, the Li evolution in the ASLMB during the charge/discharge processes remains a "black box". How the "soft short" occurs and how it impacts the Li migration in the ASLMB are still unclear.

The other challenge with Li metal anode is its plastic deformation in the ASLMB. Li metal was reported with Young's modulus of 7.82 GPa and yield strength of ≈0.8 MPa,[9] thus it tends to creep easily in ASLMBs under the pressure. Specifically, in the ASLMBs, there are two types of pressure on Li metal: the external stacking pressure and the plating-induced mechanical stress. The former is generally applied in the ASLMBs to maintain an intimate solid-solid contact.[10] According to Doux et al.,[11] the external pressure of 75 MPa on the ASLMB can immediately result in a battery short circuit while a lower pressure of 5 MPa shows acceptable cycling stability. At the same time, the plating-induced mechanical stress also affects the Li metal behavior in conjunction with the external stacking pressure. It has been reported that an overpotential of -0.135 V during plating can principally generate GPa-level hydrostatic pressure.[12] Under pressure, Li metal anode can propagate along the defects and cracks on the SE surface. Porz et al.[13] reported Li metal deposition along the surface defects inducing crack-tip stresses that propagate the cracks on the SE even further. Using in situ X-ray computed tomography (XCT), Ning et al.[4] directly observed the plating-induced cracking in ASLMB.

It is significant to visualize the Li behaviors in ASLMBs, including both "soft short" and Li metal deformation. Conventional ex situ characterization methods, such as optical microscopy and electron microscopies, are often used; however, they are prone to the risk of altering the sample structure and morphology during the process of peeling from the cell and possible exposure to the environment. Therefore, it is crucial to nondestructively visualize the Li behaviors inside the ASLMBs to correctly understand the "soft short" and Li creeping.

Herein, for the first time, we have successfully visualized the Li behavior in the ASLMBs through the combination of two nondestructive techniques, namely neutron and X-ray imagings. Neutron imaging is an ideal tool for nondestructively visualizing the Li dynamics in the ASLMBs since it has a strong capability to penetrate cell setups and a high sensitivity to Li. It can well map the Li distribution in the entire cell in a 3D view and real-time track the Li evolution during the ASLMB operation. Meanwhile, we also employed high-resolution XCT to visualize the ASLMB after the "soft short" in a 3D view. The ASLMB in the investigation was constructed with a $LiNi_{0.8}Mn_{0.1}Co_{0.1}O_2$ (NMC811) based cathode and Li metal anode. The argyrodite sulfide SE, $Li_{5.4}PS_{4.4}Cl_{1.6}$ was selected for this study as it has a remarkable ionic conductivity of 7.8 mS cm^{-1}. We successfully observed the dynamic evolution of Li in the ASLMBs before and after the "soft short" and revealed the mechano-electro-chemo behavior of Li metal. We simulated the entire cell assembly and Li deformation processes using a finite element model. Based on the findings, researchers will have more insights into the Li deformation and the "soft short" in ASLMBs, aiming to find more comprehensive strategies to stabilize the Li metal anode to achieve high-performance ASLMBs.

2. Results and Discussion

2.1. Nondestructively Visualizing All-Solid-State Li Metal Batteries through Neutron and X-Ray Imagings

Neutron and X-ray imagings are employed to nondestructively observe the ASLMB. Neutron imaging is one of the most effective methods for nondestructively investigating the Li behavior within ASLMBs. With a high sensitivity to Li, neutron imaging is capable of directly observing the Li metal morphology and quantifying the Li element evolution. Furthermore, because the neutron is highly penetrable and has rapid data acquisition capabilities, neutron imaging is capable of observing the ASLMBs in real time. Figure S1 (Supporting Information) shows the photos of the operando neutron imaging test in this work. As illustrated in **Figure 1**A, a pressurized cylindrical ASLMB can be directly used for neutron imaging and XCT. The full cell consisting of the laminated cathode, SE, and Li metal layers sandwiched between two stainless steel (SS) electrodes is enclosed in a low neutron attenuating polytetrafluoroethylene (PTFE) tube. The neutron beams transmit through the cell and are converted into optical signals which are then collected for grayscale radiograph construction.[14] The attenuation of neutron radiation is contingent upon the element species and the distance of neutron penetration paths within the cells, thereby producing a 2D radiograph image. (Figure 1B).

Figure 1C displays an example of the obtained 2D neutron radiography image and the quantified neutron transmission of the battery before the test. As a result of the high neutron total cross section (Table S1, Supporting Information), Li-related materials, especially Li metal, display dark gray colors. Figure S2 (Supporting Information) displays the magnified region of Li metal, cathode, and SE. Since the similar Li concentrations in cathode and SE, there is less contrast between them. By normalizing, we can quantify the neutron transmission from 0 to 1, thus providing a more accurate distinction. The transmission is plotted over a 2 mm length along the direction of the arrow (Figure 1C) in the region of interest. By examining the derivative plot (Figure S3, Supporting Information), it is possible to accurately pinpoint the layers and their boundaries. Furthermore, the changes in neutron transmission can be used to monitor the progress of Li evolution in different areas. Note that the PTFE tube has a slight deformation caused by the expansion of SE in the densification process under the pressure of 300 MPa. Furthermore, as shown in Figure 1D, we can determine the 3D structure of the cell through neutron/X-ray CTs when the sample is rotating at the time of collecting radiograph images. The spatial distribution of Li in ASLMB is obtained. The differences in transmission intensity between various cell states can be used to directly display the evolution of Li in a 3D representation. X-ray imaging, which can also nondestructively visualize the cell in a 3D view, is employed to cooperate with neutron imaging by taking advantage of its higher resolution. In this work, using both 2D radiography and 3D CT, we investigated the mechano- and electrochemical behavior of Li in the ASLMBs.

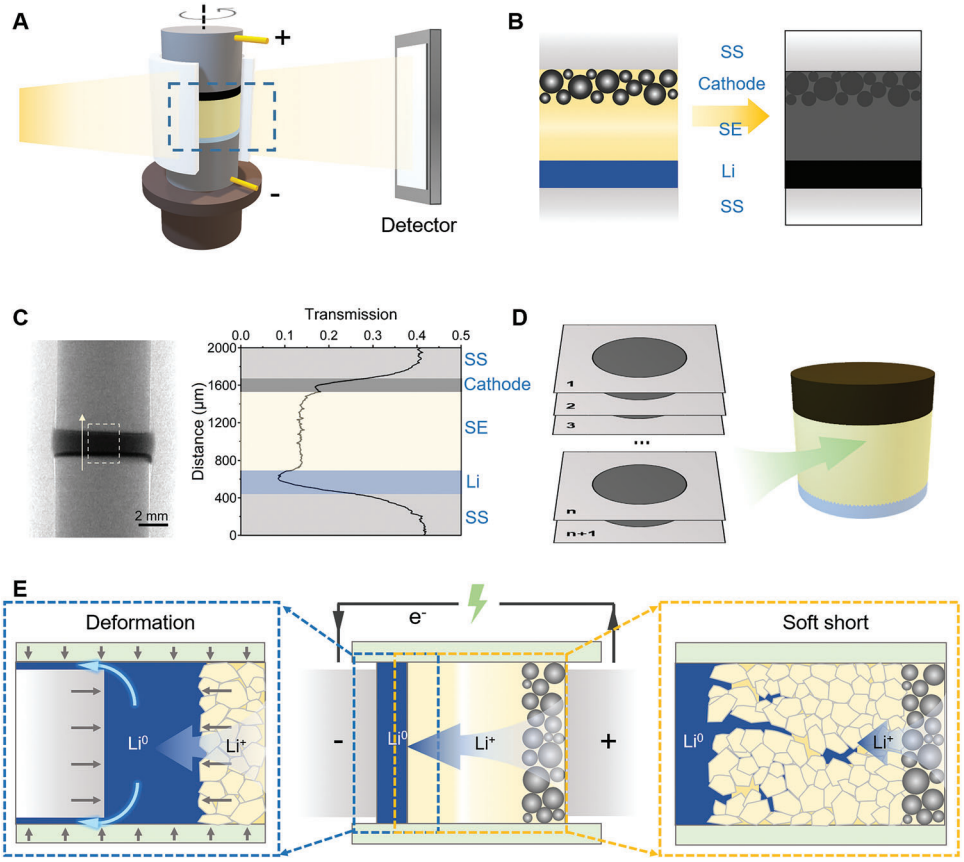

Figure 1. Investigation of the "soft short" in ASLMBs through Neutron and X-ray imagings. A) Schematic of the operando imaging investigation. B) Schematic representation of the ASLMB architecture and the neutron imaging mechanism based on the element-specific neutron attenuation. C) 2D neutron radiograph of the ASLMB, and the neutron transmission profile along the arrow direction in the marked box. D) 3D neutron and X-ray CTs of the ASLMB. E) Schematic of the Li deformation and the "soft short" caused by coupling mechano- and electrochemical reactions.

A major issue when employing Li metal anode in ASLMBs is the occurrence of deformations and dendrites. As depicted in Figure 1E, the charging procedure involves the migration of Li ions from the cathode to the anode, thereby resulting in a progressive increase in the amount of Li metal at the anode. The combination of electrochemical plating-induced stress and external stacking pressure leads to the Li moving in two directions: deformation toward the current collector side and propagation into the voids/cracks in the SE, as illustrated in Figure 1E. Meanwhile, on the SE side, the combination of electrochemical Li deposition and the mechanical stress-induced Li metal penetration caused the formation and accumulation of Li filaments, resulting in a "soft short". By combining neutron and X-ray imaging, we can nondestructively observe the evolution of Li inside ASLMBs, thus gaining a better understanding of the Li anode under high spatial and temporal resolution.

2.2. Observations Of "Soft Short" with Operando 2d Neutron Imaging

The galvanostatic charge and discharge profiles can be used to differentiate between "normal cycle", "hard short", and "soft short" in the full cell, as illustrated in Figure S4 (Supporting Information). When an ASLMB is in normal charge, Figure S4A (Supporting Information), the potential gradually increases up to the cut-off voltage as Li is released and stored in the cathode and anode, respectively. However, if the ASLMB is in a "hard short", Figure S4B (Supporting Information), its potential will rapidly decrease to near 0 V, and the voltage is unable to recover. On the other hand, when the battery is in "soft short", Figure S4C (Supporting Information), the potential fluctuates as it is being charged, indicating that both electron and ion conduction are present inside the SE[11]. In addition, the ASLMBs in "soft short" and "hard short" behave different electrochemical impedance spectra, which can be utilized to distinguish them (Figure S5, Supporting Information). It is significant to have a detailed investigation of the status of the ASLMB in a "soft short".

As the obtained raw neutron image (Figure S6, Supporting Information) suffers from the non-uniform beam structure and low statistics, an initial filtering and normalization procedure is used to remove saturated pixels and the static background, respectively. Then every 30 images are binned with the median treatment into one image to improve the signal-to-noise-ratio. **Figure 2**A displays the normalized 2D radiograph image of the ASLMB before the electrochemical cycling. We selected two regions of interest which are in the middle and edge of the battery, labeled as (I) and (II), respectively. Region I contains the richest

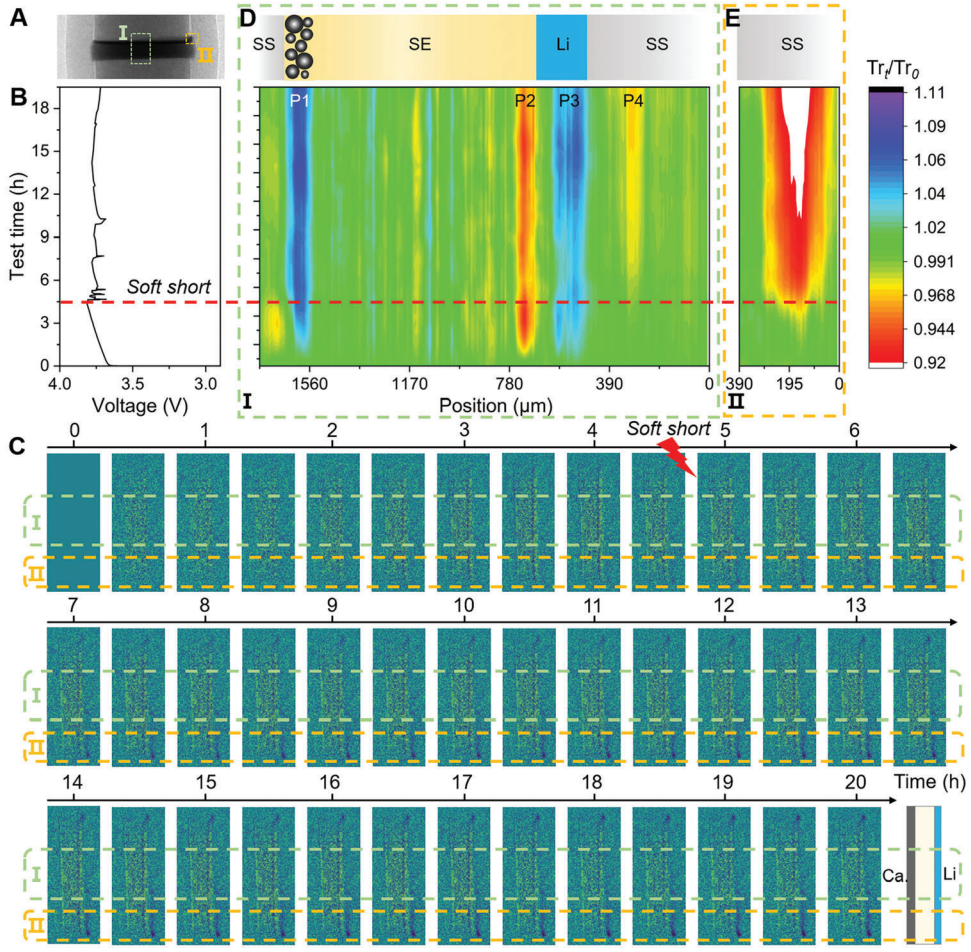

Figure 2. Operando neutron imaging investigation. A) Radiograph of the ASLMB as prepared. Two boxes demonstrate two regions of interest. B) Galvanostatic charge profile of the ASLMB to show the "soft short". C) Contrast enhancement treatment of radiographs at different charge states. The intensity mapping of the real-time transmission changes at the regions with D) green box and E) orange box. The inset schematics illustrate the cell architecture.

information of the entire cell due to the longest neutron penetration paths in this view; Region II can give more information about the Li creeping without the interruption of SS. Figure 2B displays the galvanostatic charge profile of ASLMB showing a typical "soft short" that the voltage fluctuates but dynamically maintains around 3.8 V after 4.5 h of charging. The time-stamped 2D neutron radiograph images record the Li dynamics when the battery is at the charge state (Figure S7 and Video S1, Supporting Information).

It is, however, difficult to detect the slight change due to the lack of contrast in the image. Thus, we further treat the neutron transmission in all images and get the transmission change ratio, Tr_t/Tr_0, where Tr_0 and Tr_t represent the transmissions at the beginning and at the charging time t, respectively. As shown in Figure 2C, following the contrast enhancement treatment, the colors represent Li amount evolution: bright spots show Li depletion ($Tr_t/Tr_0>1$); dark spots mean Li enrichment ($Tr_t/Tr_0<1$); Viridis color presents no Li change ($Tr_t/Tr_0 = 1$). The inset schematic illustrates the locations of the cathode and anode layers. At the anode, there is an increase in the Li concentration (increased black spots), as the battery is typically charged before the "soft short" occurs at around4.5 h. In comparison, when the battery is in a short-circuit state, the number of dark spots fluctuates, hinting that a "soft short" has happened. In the cathode, increased bright spots evidence the depletion of Li. Despite a "soft short", the brightness of the cathode persisted, confirming that the Faradic reaction continues even after a "soft short". In comparison to region I, region II exhibits a more significant darkening along the anode side, extending further toward the SS. It is hypothesized that the boost in Li metal on the SS side is due to Li metal creeping, not Li metal electrochemical plating, as this area is far from the ion conductor of SE.

We further plot the real-time evolution of Tr_t/Tr_0 in regions I and II during the test, as depicted in Figure 2D and Figure 2E, respectively. The x-axis represents the locations in the cell, and the y-axis shows the charging time. Significantly, the colors represent the Li amount variations: color more toward blue means Li depletion ($Tr_t/Tr_0>1$); color more toward red represents Li enrichment ($Tr_t/Tr_0<1$); green color depicts no Li change ($Tr_t/Tr_0 = 1$). Unfortunately, the dendrite inside the SE part was not detected, as the 2D neutron radiography displays the total neutron transmission when passing through the entire cell. The Li metal

dendrite, given its size, has a negligible influence on the sum of neutron attenuation, making it difficult to track the occurrence of "soft short".

In the cathode and anode parts, four layers own obvious Li enrichment or depletion, labeled as P1, P2, P3, and P4, separately. In the cathode side (P1 layer), there is a Li depletion during the charging process agreeing with the delithiation of NMC811. In comparison, there is a Li enrichment (P2) at the interface between SE and Li metal, which is attributed to the electrochemical Li plating and mechanical Li propagation at the anode side. The fluctuation in color intensity after 4.5 h evidences the "soft short". Notably, the Li enrichment is located at the SE near the SE|Li interface. Considering that the cold-pressed SE is porous and that there are voids and cracks on the surface (Figure S8, Supporting Information), it is evident that the plated and crept Li fills in the SE first at the interface. Once the Li metal penetrates the SE, it potentially reacts with the delithated NMC811 and sulfide SE.[15] The "soft short" causes a fluctuated increase in Li concentration at the cathode side, which results in an alternative blue color enhancing and reducing in P1 and the vibration of Tr_t/Tr_0 (Figure S9, Supporting Information). From the P1, we concluded the overall reaction in the cathode is delithiation, even after the "soft short".

Meanwhile, we observed a Li depletion layer (P3) at the anode side and a continuous Li enrichment at the cell edge (P4) and P3. This Li depletion is not in line with the expectation that the amount of Li metal would have augmented at the anode side when the battery is charged. As we will discuss in more detail later, the Li depletion layer is related to the Li deformation. Figure 2E shows an accumulation of Li in region II which is at the same position as P4 but excludes the distraction from the SS. Since this position is distanced from the SE, it implies that there is no electrochemically generated Li metal in this region. We believe that the Li creep toward the SS is caused by a combination of stacking pressure and plating-induced compression stress, as evidenced by the fact that the appearance of P3 is close to P2 at the time scale, suggesting that the deformation is not purely electrochemically induced stress.

2.3. Investigation of "Soft Short" Through X-Ray CT

To further investigate the cell failure mechanism, we conducted the high-resolution XCT on an ASLMB in a "soft short" condition. As illustrated in **Figure 3**A, the ASLMB was constructed in a homemade cell, which was utilized for the electrochemical test first and then directly implemented in XCT measurement without cell disassembly and sample extraction. Cathode, SE, and Li metal are layer-by-layer stacked in the cell, and two stainless steel rods work as the current collector. After 3 h of plating at the rate of C/20, the cell shows typical "soft short", after that the cell is further charged to 20 h (Figure S10, Supporting Information). Figure 3B displays the reconstructed 3D structure of the ASLMB. According to the grayscale contrast, the cathode, SE, and Li metal layers are clear to identify. Due to high X-ray absorption, the NMC811-based cathode shows the highest brightness after reconstruction. In comparison, Li metal exhibits a dark color after reconstruction because of the low attenuation to X-ray. The SE pallet owns a thickness of around 3 mm and a diameter of 2 mm. Noted the different contrast in SE is caused by the densification difference of SE at different regions, which widely exists in the cold-pressed sulfide SEs pallet.[16]

Five slices were taken to investigate the inner morphologies. Slice 1 was taken in a side view, while Slices 2–5 were taken in a top view at locations from cathode to anode in sequence. In Slice 1 (Figure 3C), a dendritic filament owning a low grayscale is observed growing from the Li metal anode to the cathode, while the SE in other regions is densely packed. The filament can reach 1.5 mm in height, which is longer than most reported SE thicknesses.[17] Figure 3D displays the magnified features. The filament is thin in the tip (labeled with arrows) and broad in the root, like the reported Griffith flaw in the SE.[13] Video S2 (Supporting Information) shows the continuous slices in the side view. There are many other Griffith flaws at the Li metal anode side, but none are observed at the cathode side. Considering the SE is homogeneously densified under axial pressure, these filaments are highly related to the Li metal anode and the electrochemical process. Therefore, we can predict that the Li filament starts growth from the anode side. Figure 3E compares the top view cross-section morphologies of the SE at different locations. In Slice 2, which is nearest to the cathode, most regions show dense morphology. In Slice 3, there are some scattered long filaments with lengths higher than 200 μm showing high contrast, besides the similar morphology as Slice 2. The tips should be the filaments seen in the side view image, for example in Slice 1. In the vicinity of the Li metal, as depicted in Slice 4, there are numerous filaments, some of which are interconnected. At Slice 5, a region connected to the Li metal is characterized by more filaments with wider diameters, forming a web-like structure. It is unclear if these filaments are cracks, Li metal, or a combination of the two. XCT is not able to accurately differentiate between Li metal with voids/cracks,while, the presence of either voids/cracks or Li metal will certainly reduce the battery life.

The grayscale distribution in the SE can indicate the locations and fractions of these filaments. Video S3 (Supporting Information) displays the top-view cross-section morphologies of the SE from the cathode side to the anode side. It is noticeable that the grayscale from the cathode to the anode gradually reduced. Therefore, the median grayscale values at each top-view slice are plotted from the cathode to the anode, as shown in Figure 3F. Due to the X-ray attenuation differences in different layers, the cathode, SE, and Li metal are clear to be identified in the grayscale profile. Through the derivated grayscale, the interfaces at cathode|SE and SE|anode can be well defined. Figure 3G specifically magnified the SE part to show the median grayscale distributions of the SE. The median gray scale shows an obvious reduction from the cathode side to the Li metal anode side, demonstrating that the filaments amount is correspondingly increased.

In addition, we segmentalized the ASLMB according to the gray scale differences. Figure 3H displays the 3D segmented rendering of the ASLMB. The gray color represents the NMC811 in the cathode; the yellow and brown colors represent the SE with high and low densities respectively; the black color means the randomly distributed spots with low grayscale; the red color shows the Li metal anode and the interconnected regions. Video S4 (Supporting Information) shows the 3D view of the segmented ASLMB. To better visualize the inner structure, Figure 3I only shows the regions owning a low gray scale and volume larger

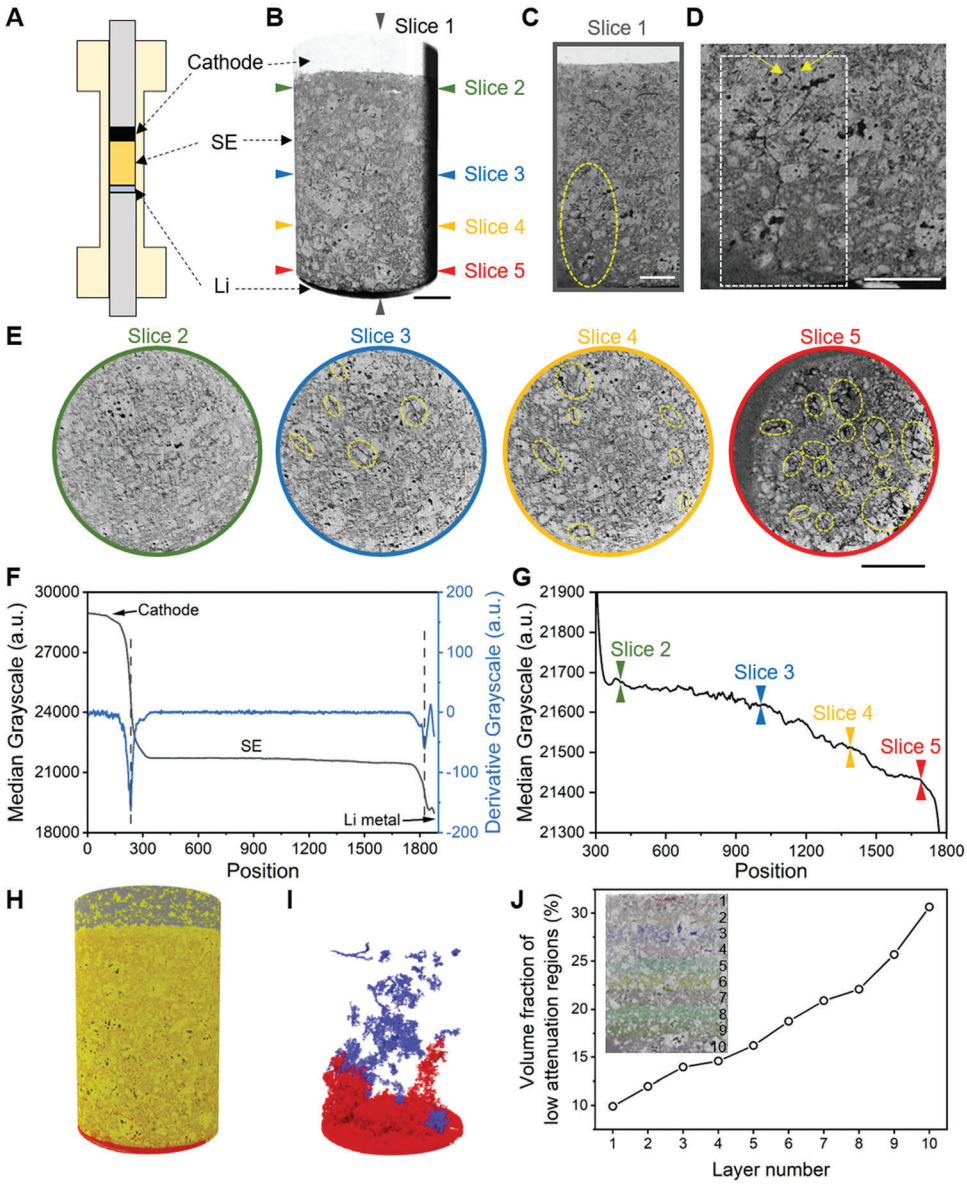

Figure 3. Ex situ XCT investigation. A) Schematic of the ASLMB configuration in XCT test. B) Reconstructed 3D structure of the ASLMB. The locations of five specific slices are labeled in the figure. C) Reconstructed 2D image of Slice 1 and the region of interest is magnified in (D). E) Reconstructed 2D images of Slices 2–5. The cracks are highlighted with yellow dash circles. F) The median grayscale in slices scanned from cathode to Li metal, and the details of the SE region are displayed in (G). 3D segmented renderings of H) ASLMB and I) Li metal-connected regions (Red), and regions showing low X-ray attenuation (Blue). J) The volume fraction distribution of regions with low X-ray attenuation within the SE. The scale bar represents 0.5 mm.

than 3.4×10^5 μm^3. There are mainly two kinds of regions: the Li metal anode and the interconnected regions (marked with red) and the regions have no connection to the Li metal (marked with blue). Evidently, these regions are mainly found on the Li metal anode side, with fewer on the cathode side (Video S5, Supporting Information). More importantly, there are large amounts of low attenuation regions that are interconnected to the Li metal anode. The farthest edge can even reach half of the SE in thickness, which agrees with the filament observed in Slice 1 in Figure 3C. Meanwhile, the regions having no connection to Li metal are scattered and take a large volume fraction in the total SE. Most of the red region consists of Li metal, while the blue region predominantly contains pores and inactive Li. However, it is a limitation of X-ray technology to accurately differentiate between pores and Li. Figure 3J plots the volume fraction of low attenuation regions in different positions in the SE which are segmentalized into 10 layers (shown in the inset image). From layer 1 to layer 10, the volume fraction of the low-attenuation regions gradually increases from 9.91 to 30.65%, agreeing with the decreased median grayscale in Figure 3G. These further demonstrate that the existence of the low-attenuation filaments is highly related to the Li metal anode.

The origin of these low-attenuation filaments is significant in understanding the "soft short" failure of the ASLMB. During plat-

ing, the Li metal creeps through the cracks in the SE, as the plating-induced stresses can drive the crack propagation followed by the Li metal propagation inside the SE.[4,13] If the Li metal within the cracks penetrates the SE throughout building a permanent connection between the cathode and Li metal anode, the cell shows a "hard short". If the Li metal within the cracks mainly distributes at the anode side and the connections between the cracks are not stably established, the cell shows a "soft short", as demonstrated in this work. In the "soft short", sometimes the connection breaks, causing the battery recovery.

2.4. Understanding the "Soft Short" through Phase Field Simulation

To further understand the underlying mechanism of the "soft short" behavior, we developed a phase-field model coupled with electrochemistry and solid mechanics theory to simulate the Li dendrite growth in a porous solid electrolyte (SE) during th electroplating process under external pressure. The simulation system consists of a Li metal anode (200 μm in thickness) and a porous SE (800 μm in thickness), while the average pore size and pore volume fraction in the SE are 10 μm and 16.25%, consistent with the experimental measurements. The Li anode phase, the solid electrolyte phase, and the pore (air) phase are well captured by the phase-field variables (see Supporting Information), and their physical properties are listed in Table S2 (Supporting Information). Four Li protrudes are introduced at Li/SE interface in the initial state to represent the Li dendrite nucleation, while a mechanical pressure (0–10 MPa) is applied on the SE side, as illustrated in Figure S11 (Supporting Information). Under the applied voltage, Li-ions diffuse and preferably deposit on these protrudes ($Li^+ + e^- = Li$) due to local field enhancement, and eventually grow into dendrite morphology. Besides, the Li plating process also induces local strains due to volume change in SE and hydrostatic pressure, giving rise to diverse Li dendrite morphology and growth modes, which eventually impact the soft short of Li metal batteries. Li dendrites and whiskers typically have sub-micrometer to micrometer scale dimensions. Previous studies have reported high yield strengths for Li at these small length scales,[18a] though exact values remain uncertain. Under the external pressures used in this work, it is believed that primarily elastic deformation of Li dendrites occurs. Thus, we make the assumption in the phase field modeling that both the Li metal and solid electrolyte experience only elastic deformation. We also assume no evolution of pores within the electrolyte during electroplating. Further mechanical testing of Li dendrites would be valuable to confirm these assumptions and accurately determine plasticity parameters.

Figures 4A–C illustrate the Li dendrite morphology, the hydrostatic pressure (P_m), and volume strain (ϵ_{vol}) in porous SE under a constant electric overpotential (−0.35 V) and different external pressures (0, 5, and 10 MPa) after 500 s of evolution. It is clearly seen that Li dendrite is suppressed with increasing external pressure. By comparing the driving forces for Li dendrite growth (Figure S12, Supporting Information), we find that the Li dendrite growth is driven by the positive chemical driving force (including bulk and electrochemical contributions, see Supporting Information) at the Li/SE interface. Meanwhile, the external pressure induces a negative elastic driving force at Li/SE interface which partially offsets the chemical driving force, thus suppressing the Li dendrite growth. From Figure 4B, the hydrostatic pressure (P_m) is maximized inside the Li dendrite. Its maximum value increases from 2 to 12 MPa as the external pressure increases, which is responsible for the suppression of Li dendrite growth. More importantly, our simulation indicates that the external pressure can cause dead Li formation. Without external pressure, Li dendrite growth is less restricted by the SE, resulting in a volume expansion (positive ϵ_{vol}) in the Li metal (Figure 4C). In addition, due to low hydrostatic pressure, Li dendrites can fill the small pores within the electrolyte and form a connected tree-like morphology. When the external pressure increases to 5 MPa, Li-ion tends to deposit along the pore-electrolyte interface, forming a network-like dendritic structure. When the external pressure reaches 10 MPa, the hydrostatic pressure in the vicinity (surface) of the pore becomes larger than that in the surrounding electrolyte. The enhanced pressure at the pore/SE interface blocks Li dendrite to fill the pores and release the partial stress. Consequently, the Li dendrites break and become dead Li during the charging process (Figure 4B; Figure S13, Supporting Information), which agrees with the experimental results (Figure 3I). The fracture of Li dendrite under large external pressure can well explain the occurrence of "soft" short as observed in Figure 2B. Without external pressure, multiple Li dendrites grow and penetrate through the entire SE, causing short circuits of Li metal batteries. This is evidenced by the sudden increase of leakage current at ≈400 s in our simulation, indicating a "hard" short (Figure 4D). In contrast, under 10 MPa external pressure, the local stress segregation in SE causes Li dendrites to break and disconnect to the anode, which avoids Li dendrite completely penetrating the SE. This is proved by the leakage current fluctuations in our simulation, indicating a typical "soft short" behavior (Figure 4D).

Another potential cause of soft shorts is Li plating inside the solid electrolyte, which can occur when the electrical conductivity of the solid electrolyte is higher than 10^{-5}-10^{-4} S cm^{-1}. We used a direct current method to measure the electrical conductivity of our solid electrolyte, which was found to be 3.2 x 10^{-9} S cm^{-1}. Therefore, we can exclude the possibility of soft shorts due to Li plating inside the solid electrolyte, since its electrical conductivity is several orders of magnitude lower than the critical value where plating would occur.

2.5. Visualization Li Metal Creeping through Neutron CT

Ex situ neutron CT is used to further track the 3D spatial evolutions of the Li distribution in the ASLMB before the cycle and after the soft short in the operando 2D neutron imaging. **Figure 5**A shows the reconstructed 3D structure of the ASLMB before cycling. We can see the SS electrode rod, Li metal, SE pallet with the cathode, and another SS electrode rod in sequence from top to bottom. The cell shows a larger diameter than the SS due to the expansion in cell stacking. This study only focused on the outermost layer of the cell, as the SS framework absorbed a considerable amount of the signals (Figure S14, Supporting Information). The outermost shell can additionally shed light on Li's morphology in the region II. After reconstructing the 3D structures of

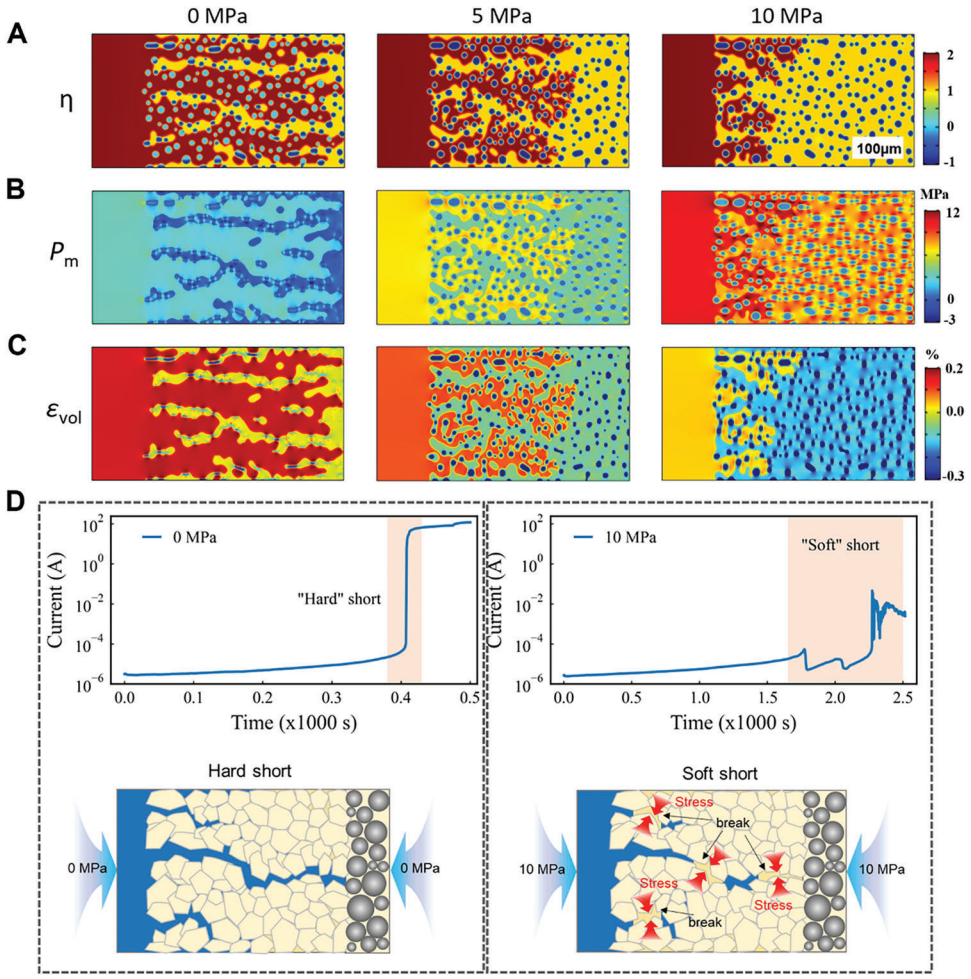

Figure 4. Phase-field simulation of Li dendrite growth in a porous electrolyte under the external pressures of 0, 5, and 10 MPa after 500 s of evolution. A) Dendrite morphology represented by η, where $\eta = 2$, 1, 0 and −1 represent the Li metal, solid electrolyte, pores filled with Li metal , and pores with air, respectively. B) Hydrostatic pressure P_m. C) Volume strain ϵ_{vol}. D) Time-dependent leakage current evolution during the charging process.

the ASLMB after the battery test (Figure S15, Supporting Information), we aligned the CT results and emphasized the regions with increased attenuation through subtraction (Figure 5B). The Li edge shows a high level of Li accumulation, which is consistent with the findings of Li deformation via 2D radiograph. By raising the attenuation threshold from 2.6 to 2.9, we effectively extracted the Li metal from the ASLMB due to its highest neutron attenuation in the cell, as demonstrated in Figure S16 (Supporting Information).

For a more comprehensive view of the evolution of the Li morphology, we have extracted cross-section images at corresponding regions using three slices (labeled Slice 1, Slice 2, and Slice 3) as shown in Figure 5C. The yellow and blue dash lines highlight the outlines of the Li cross sections before and after the test, respectively. It appears that the Li cross-section area increases after the battery electrochemical test, however, the Li outline is not simply expanding as expected. The Li amounts increased in the top region, which is evident from the expansion of the Li. Similar phenomena can be seen in the bottom region of the Li. In contrast, the Li in the middle region shrinks, suggesting a decrease in Li. We identify the positions of the Li region to the ASLMB (Figure 5D). The Li at the top region is located at the SS electrode rods; the middle region is the Li between the SS rod and SE pallet; the bottom region is at the SE pallet. As a result, the Li morphology evolution is consistent with the 2D radiography showing Li enrichment on the SS side and the Li|SE interface, and Li depletion appears on the Li|SS interface. The thinning illustrated in Figure 5 is in agreement with the P3 strip in Figure 2D. The Li amount increase in the SE and SS sides in Figure 5 corresponds to P2 and P4 in Figures 2D,E. The neutron imaging revealed thinning of the Li metal predominantly at the Li-stainless steel interface. This explained the observed signal difference between positions P2 and P3, in which P2 was caused by Li plating and P3 was due to the Li mechanic creeping. The confinement from the cell wall and stainless steel led to Li creeping toward the stainless steel side, causing Li accumulation at position P4.

2.6. Finite Element Simulation of the Li Metal Creeping

In contrast to the micron-scale dendrites, Li deformation at the current collector interface occurs on the scale of hundreds of

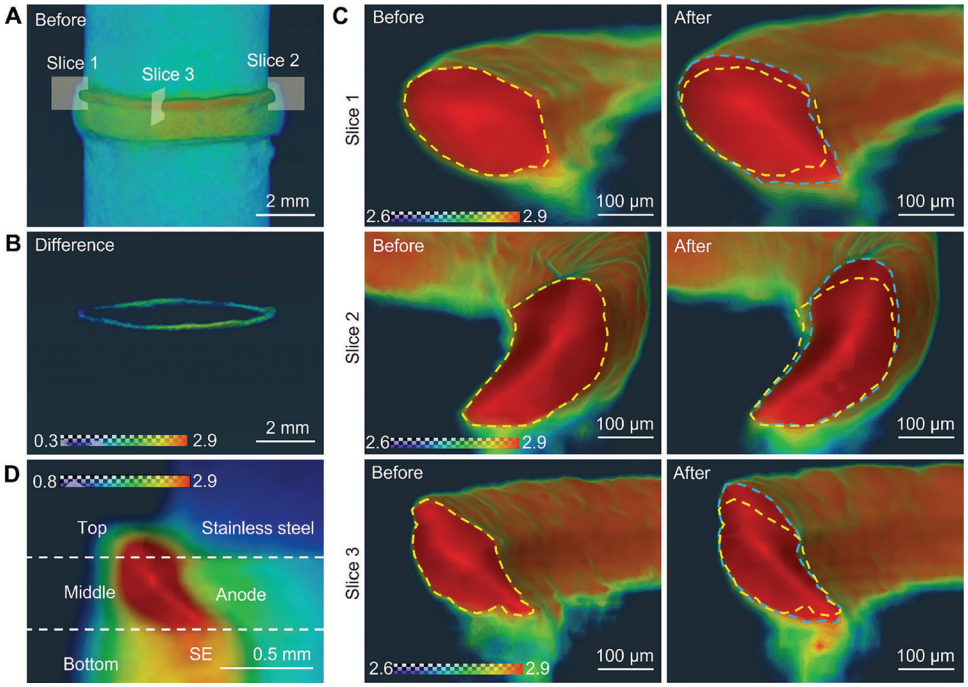

Figure 5. Ex situ neutron CT investigating of the Li metal evolution. A) 3D tomography images of the ASLMB before the battery test in Figure 2 and B) the attenuation increment. C) Zoom-in tomography images to show the morphological evolution before (left) and after (right) at slice 1, slice 2, and slice 3 marked in (A). The outlines of Li are highlighted with yellow and blue dash lines. D) 3D tomography image of the ASLMB in cross section to show the locations of different components.

micrometers to potentially millimeters scale. At these larger length scales, bulky Li is expected to have lower yield stress and exhibit plastic deformation. Therefore, for the finite element modeling of bulky Li, we implemented a viscoelastic-plastic model incorporating both elastic and plastic Li behavior. It is worth noting that different mechanical models are used in the phase field model and the finite element model, but it is not contradictory to each other because these two models are developed at different length scales and Li has a strong size effect revealed by many experimental studies.[19] Ideally, the two models should use the same mechanical model that unifies the mechanical properties of Li metal at different scales using one theory. However, till now, the Li mechanics community has not come up with such a model because more tests and fundamental understandings are still needed.

The cell assembly has a significant impact on the behavior of the Li metal in this process. Sulfide SE-based ASLMBs are generally assembled within a polyether ether ketone (PEEK)-made cell that is rigid enough (Rockwell R126) to resist deformation during the assembly process. A PTFE tube is relatively soft (durometer 50D-55D), resulting in a degree of deformation. On the other hand, PTFE has excellent neutron transparency compared to PEEK due to a low hydrogen ratio. Therefore, a PTFE tube is employed in this operando neutron imaging system. As a result of the slight deformation of the PTFE tube, a gap is created between the SS and PTFE, which alters the behavior of Li.

A finite element model was developed to investigate the deformation of the components in the assembled ASLMB, especially the Li metal. To fully understand the contribution of mechanical deformation, we simulated all three steps that undergo mechanical loading (Video S6, Supporting Information), including 1) the SE densification (compressing SE under 300 MPa pressure), 2) ASLMB stacking (compressing with 10 MPa pressure), and 3) charge process (expansion due to lithium plating). **Figure 6** shows the simulation results. During the SE densification step (Figures 6A,B), SE is dramatically densified and develops high internal stress. The PTFE tube deforms plastically due to its relatively low yield stress, resulting in a significant bulge in the tube and a small gap between the tube and the SE (Figure 6B), as observed in the experiments. After assembling the cell and applying 10 MPa pressure (Figure 6C), the Li metal shows significant plastic deformation because of its low yield stress (Figure 6E) and flows to fill the gap. Mechanical deformation is also seen during charge because new Li plates on the interface and the overall Li foil tends to expand through the thickness during plating. However, this expansion is constrained by the fixed SS-made cell framework. As a result, the Li metal further deforms and flows deeper into the gap to accommodate the expansion (Figure 6D), which agrees with the observed Li enrichment at region II in Figure 2E. Meanwhile, the pressure inside the cell gradually rises during the charging process (Figure 6F). Figure 6G shows a comparison of the Li foil deformation before and after the charge, which is consistent with the observations in Figure 3. Details of the simulation setup can be found in the Supporting Information.

3. Conclusion

For the first time, this study successfully implemented operando neutron imaging and XCT to nondestructively observe the Li

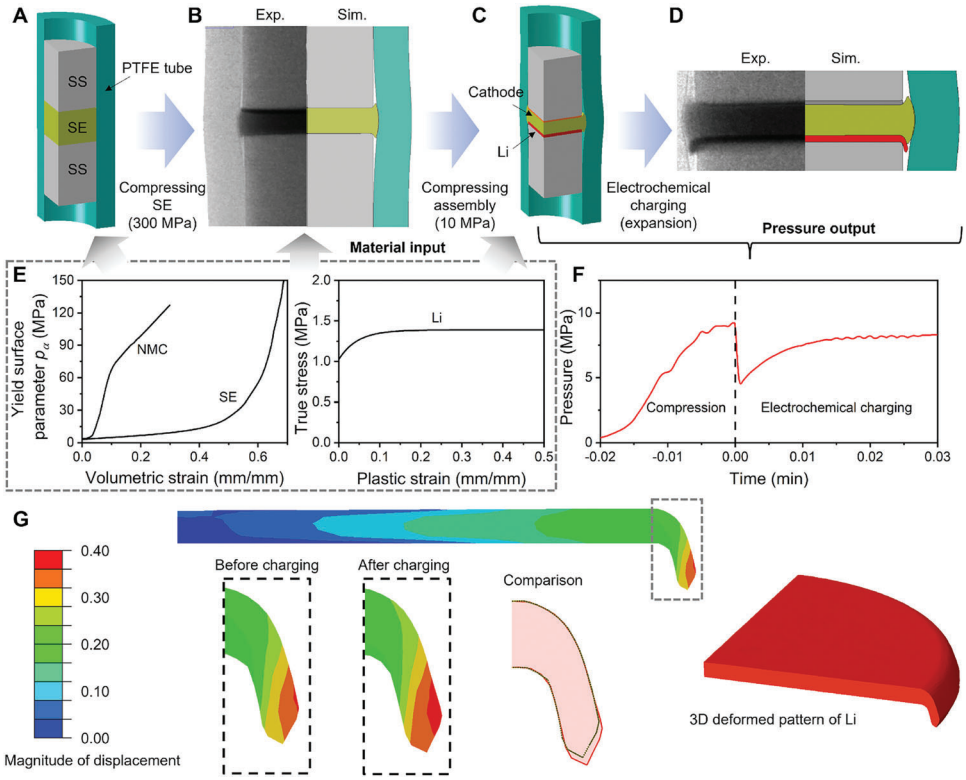

Figure 6. Finite element simulation of the mechanical deformation during the entire manufacturing-testing process. A) Simulation setup for SE manufacturing. B) Comparison of deformed configuration after SE manufacturing between experiment and simulation. C) Deformation of the SE is transferred to a new simulation model for cell assembly. D) After re-compression, the cell is charged. E) Material property inputs for the FE models. F) Internal pressure output from the final simulation. G) Deformation pattern of the lithium foil before and after charging.

dendrite-caused "soft short" and the deformation of bulky Li in ASLMBs. 2D neutron radiography provides a real-time view of the Li evolution throughout the battery, while 3D neutron CT visualizes the Li metal deformation and XCT visualizes the Li dendrite evolution inside the SE. As illustrated in **Figure 7**, as the battery is charged at the initial plating stage, Li immigrates from the cathode and deposits at the interface between Li metal and the SE. The "soft short" occurs and is accompanied by the fluctuation of Li loss and increase on both the cathode and anode attributed to the coupling of mechano- and electrochemical- reactions. This work reveals that Faradaic reactions persist in the battery, even when the ASLMB has gone through a "soft short".

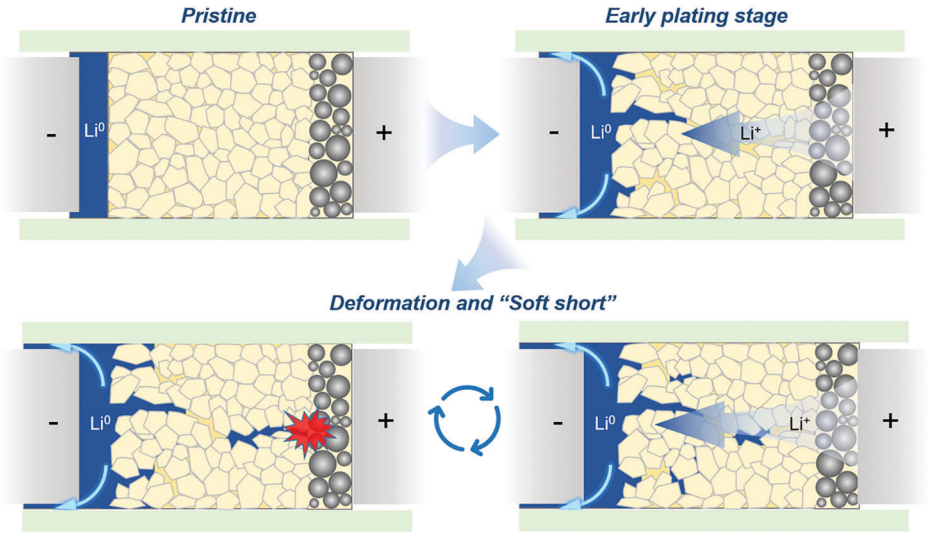

Figure 7. Mechano-electrochemical reactions induced Li deformation and "soft short".

3D tomography evidences that the Li anode thins during deformation, explaining the Li depletion region P3 observed in the Neutron 2D radiography on the anode side during charge. The plating-induced stress, in conjunction with the stacking pressure, leads to the Li metal creeping toward the pre-existing defective edge region of the cell wall.

By combining phase-field modeling with electrochemistry and solid mechanics theory, our team developed a comprehensive simulation of lithium dendrite growth under the subtle effects of external pressure. This work elucidates the previously perplexing "soft short" phenomenon seen in sulfide solid electrolytes. Our research makes clear that external pressure acts as a barrier to dendrite growth and can also cause dendrite fractures. This crucial finding thus explains the origins of both "soft" and "hard" shorts in Li metal batteries. Our investigative efforts underline that Li plating and the "soft short" phenomena are not isolated events, but rather the result of complex interactions between mechanical- and electrochemical- reactions within all-solid-state batteries. Moving forward, one focus of future research in sulfide all-solid-state Li metal batteries should be on minimizing pressure within the Li metal anode, thereby offering a means to control Li deformation and growth, ultimately improving battery performance.

4. Experimental Section

Materials: The sulfide solid electrolyte used in this work was $Li_{5.4}PS_{4.6}Cl_{1.4}$, which has been reported in the previous work.[20] The ionic conductivity was 7.8 mS cm^{-1}. The cathode active material was a Li_2SiO_x coated single-crystal NMC811 (Nanoramic Inc, USA), as synthesized through a wet chemical method.[21] The weight ratio of Li_2SiO_x is 2 wt.%. The cathode was composed of Li_2SiO_x coated NMC811, $Li_{5.4}PS_{4.6}Cl$, and vapor-grown carbon fiber in a weight ratio of 80:20:2, which are mixed in a ball milling at 150 rpm for 1 h. The Li metal foil (Fisher Scientific, USA) was thinned to ≈250 µm through pressing.

Electrical Conductivity of Solid Electrolyte: The electronic conductivity of the solid electrolyte was measured by the direct-current polarization method. 126 mg of SE was pressed under 300 MPa in a homemade cell with a diameter of 12.6 mm by two stainless-steel ion-blocking electrodes. The polarization voltage was 0.5 V with a test pressure of 50 MPa. The steady-state current (SSC) was collected after 20 min.

Cell Fabrication for Neutron Imaging: The battery was assembled in a Polytetrafluoroethylene-made tube with a diameter of 1/4 inch inner diameter. In detail, 60 mg of $Li_{5.4}PS_{4.6}Cl_{1.4}$ powders were pressed inside the PTFE tube under a pressure of 300 MPa for 10 min. Two SS rods with a diameter of 1/4 inch worked as the plugs. Then 8 mg of cathode powder was cast onto one side of the $Li_{5.4}PS_{4.6}Cl_{1.4}$ pallet and further pressed at a pressure of 100 MPa. A piece of Li with a diameter of 1/4 inch was pressed onto one SS plug by hand and then placed on the other side of the $Li_{5.4}PS_{4.6}Cl_{1.4}$ pallet. An external pressure of 10 MPa was applied in the cell and fixed with an SS-made framework.

Operando Neutron Imaging Experiment: The neutron imaging was operated at the cold neutron imaging beamline, CG1D, at the High Flux Isotope Reactor, Oak Ridge National Laboratory. The polychromatic cold neutron beam owned a wavelength of range from 0.8 to 6 Å and a peak intensity of 2.2×10^6 n cm^{-2} s^{-1} at 2.6 Å. The detector-to-pinhole distance was 6.59 m. The pinhole diameter was 11 mm. The resulting spatial resolution was 25 µm. The cell was placed between the detector and the neutron beam. The transmitted neutron was collected by a scientific Complementary Metal-Oxide-Semiconductor (sCMOS) camera system (Zyla5.5, Andor Technology plc. Belfast, UL) with a 20 µm thick Gd_2O_2S : Tb scintillator screen. In the operando test, the cell was fixed and the real-time 2D radiography was collected every 10 s. Before and after the battery test, a 3D computed tomography was conducted using another setup (Andor iKon-L 936) with 75–100 µm spatial resolution. The cell autorotated with a step size of 0.65°, and the exposure time was 20 s for images recorded at each step. The cell was charged at C/20 (1C = 200 mA $g_{NMC811}{}^{-1}$) for 20 h.

Normalization of the Transmission Neutron Radiographs: The normalization of the raw images was conducted with the Jupyter Imaging Notebook developed by ORNL. The saturated pixels and background noise were corrected first. The open beam and dark field images were collected for normalization. The neutron transmission, $I_N(i, j)$, could be normalized in the range from 0 to 1 through

$$I_N\ (i,\ j) = \frac{I\ (i,j) - DF\ (i,j)}{OB\ (i,j) - DF\ (i,j)} \tag{1}$$

where $I(i, j)$, $OB\ (i, j)$, and $DF\ (i, j)$ represent the raw neutron intensity, open beam intensity, and dark field intensity, respectively. Then every 30 images are averaged through a median method to enhance the signal-to-noise ratio. So, the time resolution is 5 minutes for one image.

Neutron Computed Tomography Images Analysis: Volume reconstruction was performed using MuhRec.[22] The 3D visualization and geometry reconstruction of the neutron computed tomography images were operated with the commercially available AMIRA software.[23]

X-ray Computed Tomography (XCT): The battery was assembled in a PEEK-made tube with a diameter of 2 mm inner diameter. 15 mg of SE was densified inside the tube first by two stainless steel rods under axial pressure. Then 1 mg of cathode powder was cast onto one side. A piece of Li in diameter of 2 mm was attached to the other side. The stainless steel rods were fixed onto the PEEK tube through a screw connection, which could apply external stacking pressure to the battery during the test. The battery was charged at C/20.

The XCT data collection was conducted using a Zeiss Xradia Versa 520 XCT unit, operated at 60 kV and 83.6 µA. The XCT data were acquired from a sample rotation of 360° (vertical axis) with 1601 projections at equal steps. A 1 × 1 binning on the detector side was used to maximize resolution. The voxel size was 1.62 µm with the 4x objective. For image processing and segmentation, the Fiji software v. 2.9.0 and ORS Dragonfly PRO v.3.5 software were used.

Phase Field Simulation Method: To describe the microstructure of the system, two continuous phase field variables were employed to define three phases with ($\eta = 2$: $\xi = 1$, $\rho = 1$) for Li metal, ($\eta = 1$: $\xi = 0$, $\rho = 1$) for the solid electrolyte, and ($\eta = -1$: $\xi = 0$, $\rho = -1$) for pores. The total free energy (F) includes the chemical, gradient, electrostatic, and elastic energy, i.e.,

$$F = \int_V [f_{ch}(\xi, \rho, c_i^*) + f_{grad}(\nabla\xi, \nabla\rho) + f_{elec}(c_i^*, \varphi) + f_{elas}(e_{ij}, \xi)]dV \tag{2}$$

where c_i^* is a set of dimensionless concentration of species, (i.e., i = Li^+, e^-), φ is the electrostatic potential, and e_{ij} denotes the elastic strain tensor. The details of each energy contribution term can be found in Supporting Information. The temporal evolutions of ξ and ρ are simulated by solving the Allen-Cahn equation incorporating Butler-Volmer kinetics[24] and the conventional Cahn–Hilliard equation as,[25]

$$\begin{aligned} \frac{\partial\xi}{\partial t} &= -L_\xi\left[\frac{\partial f_{ch}(\xi)}{\partial\xi} - \kappa_\xi\nabla^2\xi + \frac{\partial f_{elas}(\xi)}{\partial\xi}\right] - L_\eta h'(\xi)\left\{c_{Li}^* \exp\left[\frac{(1-\alpha)F\eta}{RT}\right] - c_{Li^+}^* \exp\left[-\frac{\alpha F\eta}{RT}\right]\right\} \\ \frac{\partial\rho}{\partial t} &= \nabla\left(M(\rho)\nabla\left(\frac{\partial f_{ch}(\rho)}{\partial\rho} - \kappa_\rho\nabla^2\rho\right)\right) \end{aligned} \tag{3}$$

where L_ξ and $M(\rho)$ are the interfacial mobility coefficients for ξ and ρ, L_η is the reaction rate coefficient, $h(\xi) = \xi^3(6\xi^2 - 15\xi + 10)$ is an interpolating function to limit the driving force at the interface of electrode and electrolyte, η is the overpotential of the reaction, α and $1 - \alpha$ are the charge transfer coefficients, κ_ξ and κ_ρ are the gradient energy coefficients. The phase evolution (Equations 2 and 3) are solved simultaneously with mass transport (Equation S2, Supporting Information), electrostatic distribution (Equation S3, Supporting Information) and mechanical equilibrium equation (Equation S4, Supporting Information) as detailed in Supplementary Materials. All phase-field simulations were calculated by a finite

element solver COMSOL Multiphysics. 2D models with a size of 1000 μm × 500 μm were built in this work, as shown in Figure S10 (Supporting Information). The simulation domain was discretized by physical extremely fine mesh size for improving the convergence and accuracy. The voltage applied on the left boundary and right boundary were set as −0.35 and 0 V. The external pressure is applied on the right boundary and the left boundary is fixed. Detailed boundary conditions and the parameters used in the phase field model are found in Figure S10 and Table S2 (Supporting Information).

Supporting Information

Supporting Information is available from the Wiley Online Library or from the author.

Acknowledgements

This research used resources at the High Flux Isotope Reactor, a DOE Office of Science User Facility operated by the Oak Ridge National Laboratory. The authors acknowledge Dr. Jean Bilheux for the developed Jupyter Imaging Notebook. H.Z. acknowledges the financial support from National Science Foundation under Award Number CBET-ES-1924534. Y.C. acknowledges the financial support from the National Science Foundation under Award Number 2038083. The research performed by J.Z. and W.L. was partially supported by the NASA Ames Research Center through the 19-TTT-0103 program (No. 80NSSC21M0114). We acknowledge Dr. Arturas Adomkevicius for editing.

This manuscript has been authored by UT-Battelle, LLC under Contract No. DE-AC05-00OR22725 with the U.S. Department of Energy. The United States Government retains the publisher, by accepting the article for publication, acknowledges that the United States Government retains a non-exclusive, paid-up, irrevocable, world-wide license to publish or reproduce the published form of this manuscript, or allow others to do so, for United States Government purposes. The Department of Energy will provide public access to these results of federally sponsored research in accordance with the DOE Public Access Plan (http://energy.gov/downloads/doe-public-access-plan).

Conflict of Interest

The authors declare no conflict of interest.

Author Contributions

D.C. and K.Z. contributed equally to this work. The manuscript was written through contributions of all authors. All authors have given approval to the final version of the manuscript.

Data Availability Statement

The data that support the findings of this study are available from the corresponding author upon reasonable request.

Keywords

Li metal, mechano-electrochemical reaction, operando neutron imaging, soft short, solid-state batteries

Received: July 12, 2023
Revised: August 28, 2023
Published online:

[1] a) H. Yuan, X. Ding, T. Liu, J. Nai, Y. Wang, Y. Liu, C. Liu, X. Tao, *Mater. Today* **2022**, *53*, 173; b) C.-P. Yang, Y.-X. Yin, S.-F. Zhang, N.-W. Li, Y.-G. Guo, *Nat. Commun.* **2015**, *6*, 8058; c) D. Lin, Y. Liu, Y. Cui, *Nat. Nanotechnol.* **2017**, *12*, 194; d) X.-B. Cheng, R. Zhang, C.-Z. Zhao, Q. Zhang, *Chem. Rev.* **2017**, *117*, 10403.
[2] D. Cao, X. Sun, Q. Li, A. Natan, P. Xiang, H. Zhu, *Matter* **2020**, *3*, 57.
[3] E. J. Cheng, A. Sharafi, J. Sakamoto, *Electrochim. Acta* **2017**, *223*, 85.
[4] Z. Ning, D. S. Jolly, G. Li, R. De Meyere, S. D. Pu, Y. Chen, J. Kasemchainan, J. Ihli, C. Gong, B. Liu, D. L. R. Melvin, A. Bonnin, O. Magdysyuk, P. Adamson, G. O. Hartley, C. W. Monroe, T. J. Marrow, P. G. Bruce, *Nat. Mater.* **2021**, *20*, 1121.
[5] F. Shen, M. B. Dixit, X. Xiao, K. B. Hatzell, *ACS Energy Lett.* **2018**, *3*, 1056.
[6] F. Han, A. S. Westover, J. Yue, X. Fan, F. Wang, M. Chi, D. N. Leonard, N. J. Dudney, H. Wang, C. Wang, *Nat. Energy* **2019**, *4*, 187.
[7] W. Ping, C. Wang, Z. Lin, E. Hitz, C. Yang, H. Wang, L. Hu, *Adv. Energy Mater.* **2020**, *10*, 2000702.
[8] C. Wang, T. Deng, X. Fan, M. Zheng, R. Yu, Q. Lu, H. Duan, H. Huang, C. Wang, X. Sun, *Joule* **2022**, *6*, 1770.
[9] A. Masias, N. Felten, R. Garcia-Mendez, J. Wolfenstine, J. Sakamoto, *J. Mater. Sci.* **2019**, *54*, 2585.
[10] Y. Su, L. Ye, W. Fitzhugh, Y. Wang, E. Gil-González, I. Kim, X. Li, *Energy Environ. Sci.* **2020**, *13*, 908.
[11] J.-M. Doux, H. Nguyen, D. H. S. Tan, A. Banerjee, X. Wang, E. A. Wu, C. Jo, H. Yang, Y. S. Meng, *Adv. Energy Mater.* **2020**, *10*, 1903253.
[12] Y. Chen, Z. Wang, X. Li, X. Yao, C. Wang, Y. Li, W. Xue, D. Yu, S. Y. Kim, F. Yang, A. Kushima, G. Zhang, H. Huang, N. Wu, Y.-W. Mai, J. B. Goodenough, J. Li, *Nature* **2020**, *578*, 251.
[13] L. Porz, T. Swamy, B. W. Sheldon, D. Rettenwander, T. Frömling, H. L. Thaman, S. Berendts, R. Uecker, W. C. Carter, Y.-M. Chiang, *Adv. Energy Mater.* **2017**, *7*, 1701003.
[14] Y. Zhang, K. S. R. Chandran, H. Z. Bilheux, *J. Power Sources* **2018**, *376*, 125.
[15] B. Song, I. Dhiman, J. C. Carothers, G. M. Veith, J. Liu, H. Z. Bilheux, A. Huq, *ACS Energy Lett.* **2019**, *4*, 2402.
[16] a) D. Cao, Q. Li, X. Sun, Y. Wang, X. Zhao, E. Cakmak, W. Liang, A. Anderson, S. Ozcan, H. Zhu, *Adv. Mater.* **2021**, *33*, 2105505; b) J. A. Lewis, F. J. Q. Cortes, Y. Liu, J. C. Miers, A. Verma, B. S. Vishnugopi, J. Tippens, D. Prakash, T. S. Marchese, S. Y. Han, C. Lee, P. P. Shetty, H.-W. Lee, P. Shevchenko, F. De Carlo, C. Saldana, P. P. Mukherjee, M. T. McDowell, *Nat. Mater.* **2021**, *20*, 503.
[17] S. Randau, D. A. Weber, O. Kötz, R. Koerver, P. Braun, A. Weber, E. Ivers-Tiffée, T. Adermann, J. Kulisch, W. G. Zeier, F. H. Richter, J. Janek, *Nat. Energy* **2020**, *5*, 259.
[18] a) L. Zhang, T. Yang, C. Du, Q. Liu, Y. Tang, J. Zhao, B. Wang, T. Chen, Y. Sun, P. Jia, H. Li, L. Geng, J. Chen, H. Ye, Z. Wang, Y. Li, H. Sun, X. Li, Q. Dai, Y. Tang, Q. Peng, T. Shen, S. Zhang, T. Zhu, J. Huang, *Nat. Nanotechnol.* **2020**, *15*, 94; b) C. Xu, Z. Ahmad, A. Aryanfar, V. Viswanathan, J. R. Greer, *Proc. Natl. Acad. Sci. U. S. A.* **2016**, *114*, 57.
[19] C. D. Fincher, D. Ojeda, Y. Zhang, G. M. Pharr, M. Pharr, *Acta Mater.* **2020**, *186*, 215.
[20] X. Sun, D. Cao, Y. Wang, T. Ji, W. Liang, H. Zhu, *Adv. Mater. Interfaces* **2022**, *9*, 2200539.
[21] D. Cao, X. Sun, Y. Li, A. Anderson, W. Lu, H. Zhu, *Adv. Mater.* **2022**, *34*, 2200401.
[22] A. P. Kaestner, *Nucl. Instrum. Methods Phys. Res., Sect. A* **2011**, *651*, 156.
[23] D. Stalling, M. Westerhoff, H.-C. Hege, presented at The Visualization Handbook **2005**.
[24] a) X. Shen, R. Zhang, P. Shi, X. Chen, Q. Zhang, *Adv. Energy Mater.* **2021**, *11*, 2003416; b) Y. Ren, K. Zhang, Y. Zhou, Y. Cao, *ACS Appl. Mater. Interfaces* **2022**, *14*, 30658.
[25] J.-M. Hu, B. Wang, Y. Ji, T. Yang, X. Cheng, Y. Wang, L.-Q. Chen, *ACS Appl. Mater. Interfaces* **2017**, *9*, 33341.